

PART OF A SPECIAL ISSUE ON FUNCTIONAL–STRUCTURAL PLANT MODELLING

Modelling biomechanics of bark patterning in grasstrees

Holly Dale^{1,*}, Adam Runions², David Hobill¹ and Przemyslaw Prusinkiewicz^{2,*}

¹Department of Physics and Astronomy and ²Department of Computer Science, University of Calgary, AB T2N 1N4, Canada

* For correspondence. E-mail hjdale@ucalgary.ca or pwp@cpsc.ucalgary.ca

Received: 15 November 2013 Returned for revision: 3 February 2014 Accepted: 3 July 2014 Published electronically: 13 August 2014

- **Background and Aims** Bark patterns are a visually important characteristic of trees, typically attributed to fractures occurring during secondary growth of the trunk and branches. An understanding of bark pattern formation has been hampered by insufficient information regarding the biomechanical properties of bark and the corresponding difficulties in faithfully modelling bark fractures using continuum mechanics. This study focuses on the genus *Xanthorrhoea* (grasstrees), which have an unusual bark-like structure composed of distinct leaf bases connected by sticky resin. Due to its discrete character, this structure is well suited for computational studies.
- **Methods** A dynamic computational model of grasstree development was created. The model captures both the phyllotactic pattern of leaf bases during primary growth and the changes in the trunk's width during secondary growth. A biomechanical representation based on a system of masses connected by springs is used for the surface of the trunk, permitting the emergence of fractures during secondary growth to be simulated. The resulting fracture patterns were analysed statistically and compared with images of real trees.
- **Key Results** The model reproduces key features of grasstree bark patterns, including their variability, spanning elongated and reticulate forms. The patterns produced by the model have the same statistical character as those seen in real trees.
- **Conclusions** The model was able to support the general hypothesis that the patterns observed in the grasstree bark-like layer may be explained in terms of mechanical fractures driven by secondary growth. Although the generality of the results is limited by the unusual structure of grasstree bark, it supports the hypothesis that bark pattern formation is primarily a biomechanical phenomenon.

Key words: Functional–structural plant modelling, bark pattern, fracture mechanics, primary growth, secondary growth, biomechanical model, phyllotaxis, *Xanthorrhoea*, grasstree.

INTRODUCTION

Xanthorrhoea, commonly known as the grasstree (Fig. 1), is a genus of monocots native to Australia. There are 28 species of grasstrees, some of which (e.g. *Xanthorrhoea johnsonii*, *glauca* and *latifolia*) develop an arborescent trunk (Lamont *et al.*, 2004). The main apex of the grasstree periodically produces terminal inflorescences; consequently, vegetative growth is sympodial, with an auxiliary bud taking over further development (Gill and Ingwersen, 1976). The production of an inflorescence can create bends or kinks in the trunk (Bülow-Olsen *et al.*, 1982) that modify the otherwise cylindrical appearance of the trunk.

The morphology of grasstrees is adapted to withstand and respond to frequent fires. Their leaves are arranged into dense spiral phyllotactic patterns (Staff, 1968). During fires, leaves are burnt back to their bases, resulting in the melting of a sticky resin produced by the plant. The solidification of this resin cements the burnt leaf bases together, forming a 'stem sheath' (Colangelo *et al.*, 2002) or bark-like layer of diamond-shaped leaf bases (Fig. 2) that protects the tree from diseases and future fires (Lamont *et al.*, 2004).

Grasstrees have an unusual characteristic for monocots in that they have a secondary thickening meristem (Rudall, 1991). This leads to the growth of the trunk in diameter, which, as a geometric necessity, increases the distances between the leaf bases. As a

result, the regular lattice of interconnected leaf bases may break into patches that resemble bark patterns observed in other trees. In our study, we have focused on old (hundreds of years) and large (reaching 5 m in height) grasstrees on Mount Kiangarow in the Bunya Mountains National Park, Queensland, Australia, in which such bark patterns are common. The dominant pattern consists of highly elongated, predominantly vertical patches of interconnected leaf bases (Fig. 2C). In some trees, or tree regions, the pattern has a more reticulate character. In this case, patches are smaller and less anisotropic (Fig. 2B). The difference in patterns appears to be correlated with the observed difference in leaf base shape between the two areas (Fig. 2D–H).

Here we show that the development of grasstree bark patterns can be explained as a result of mechanical fractures that emerge in the resin connecting leaf bases as the trunk grows in girth. To demonstrate this, we have constructed a virtual grasstree that combines a geometric model of primary and secondary tree growth with a mechanical model of fractures. The natural grid resulting from the phyllotactic arrangement of leaf bases offers a unique opportunity to simulate fractures using a simple discrete model. By changing model parameters, we have been able to reproduce the range of patterns observed in the grasstrees used in our study.

Historically, fractures in different materials have been simulated using both discrete and continuous models. Skjeltop and Meakin (1988) introduced a mass-spring model to simulate



FIG. 1. Young and mature grasstrees.

fractures in an elastic layer under tension. They used a triangular mesh of masses connected by springs and attached each mass to an underlying substrate layer by another spring. To simulate shrinking in the material, their simulation started with the top layer stretched isotropically (already under tension) and the connecting springs were broken probabilistically depending on the difference between the actual length of the spring and the rest length. These fracture patterns were further analysed by Morgenstern *et al.* (1993) for a one-dimensional grid and Bohn *et al.* (2005) for continuous media. To model fractures in tree bark, Federl and Prusinkiewicz (1996) adopted the system proposed by Skjetorp and Meakin. They modelled the bark as a bi-layered system with the outer layer of the tree being stretched radially by the inner live tissue. In contrast to the work presented here, they considered the mass-spring model as an (imperfect) discrete approximation of bark that consisted of a homogeneous material. Improving this approximation, Federl and Prusinkiewicz (2004) modified their previous model by replacing the masses and springs with a finite-element method. The resulting model produced plausible bark patterns, but the question of whether real bark is adequately approximated as a continuous, homogeneous sheet was not addressed.

MATERIALS AND METHODS

Grasstree simulation

Our work focused on the emergence of fractures that transform the initial phyllotactic arrangement of leaf bases into a structure with a bark-like appearance.

Phyllotactic pattern generation. The simplest method for generating the initial arrangement of leaf bases would make use of the

geometric characterization of phyllotaxis as a regular lattice on the surface of a cylinder (Erickson, 1983; Van Iterson, 1987; Prusinkiewicz and Lindenmayer, 1990). However, our model also incorporates the dome-shaped apical part of the trunk that supports leaves. This dome is modelled as a surface of revolution, obtained by rotating a graphically defined profile curve around the tree axis (Fig. 3). At its base, the dome is connected to the cylindrical trunk. All leaves were positioned using the Ridley (1986) model of phyllotaxis, previously applied to computational modelling by Prusinkiewicz *et al.* (2001). Ridley's model packs organs on the supporting surface by assuming a fixed divergence angle and by displacing the organs vertically according to the area that they occupy. In our implementation, Ridley's model operates dynamically, with new leaves inserted at the tip of the apical dome as the space becomes available for them. This increase is a joint effect of primary and secondary growth.

Growth simulation. Primary growth is simulated by increasing the height of the tree linearly as a function of time. Secondary growth is simulated by assuming that the area of the trunk cross-section increases linearly with time, and thus the radius increases as the square root of the plant's age. This assumption is loosely motivated by the pipe model (Shinozaki *et al.*, 1964a, b), according to which a linearly growing number of vascular strands connecting leaves to the base of the tree would result in linear growth in the cross-sectional area of the trunk. We obtained the same results by increasing the trunk radius, rather than cross-section, linearly with age. We limited our simulations to older trees, as our data only show bark patterns in such trees.

We calibrated the length and time variables used in our model by assuming that approximately 412.5 leaves grow per year (Bülow-Olsen *et al.*, 1982) and the trunk typically elongates by

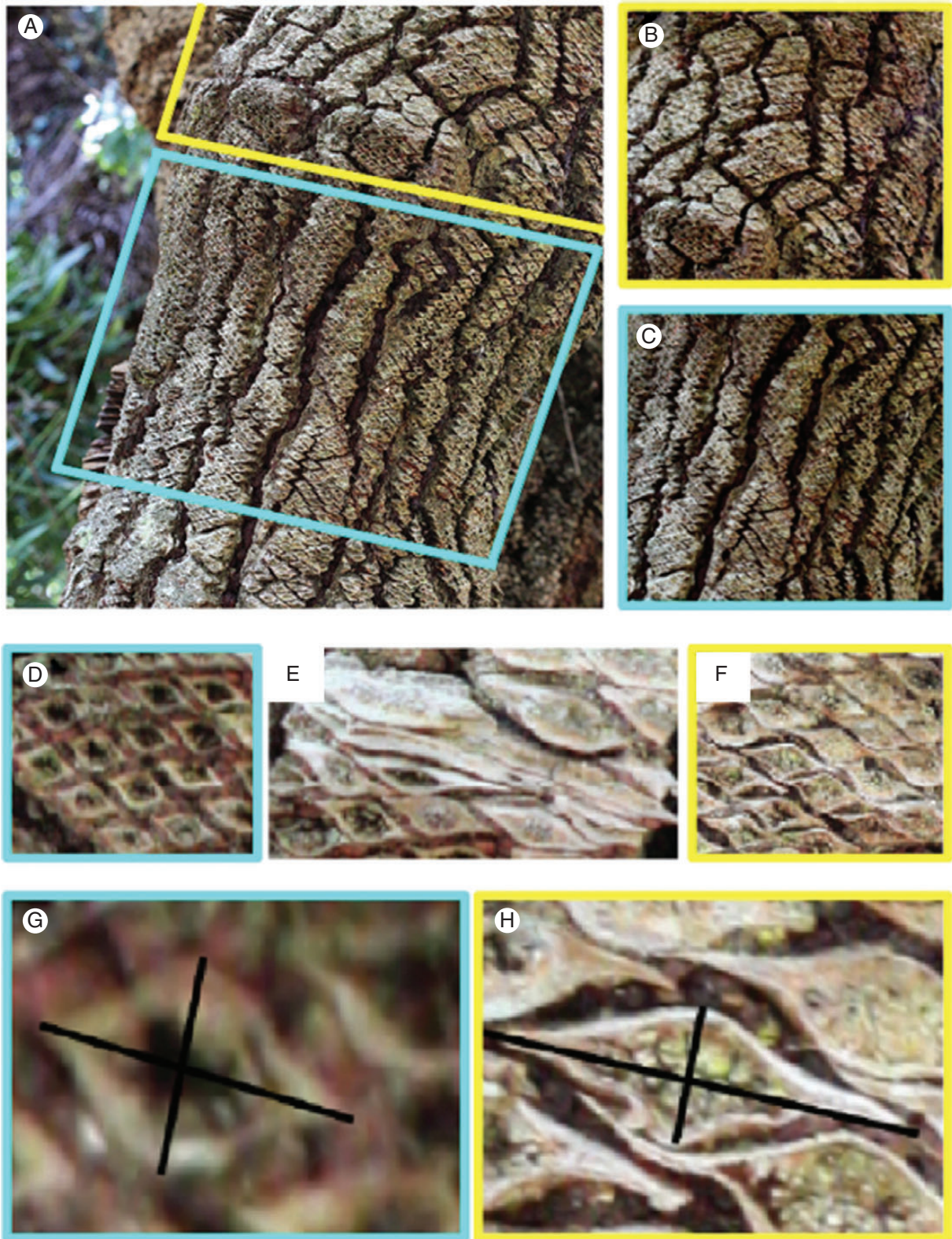


FIG. 2. Section of a grasstree trunk with a bend in the trunk. (A) The two areas enclosed in coloured boxes have different leaf base geometries. The yellow box indicates a region with reticulate fractures and the blue box indicates a region with elongated fractures. (B, C) Isolated images of a reticulate pattern (B) and an elongated pattern (C). (D–H) Leaf bases in the region with elongated fractures are more equilateral (D, G), whereas leaf bases at the bend of the trunk are severely deformed (E) and leaf bases in the region with reticulate fractures are horizontally stretched (F, H).

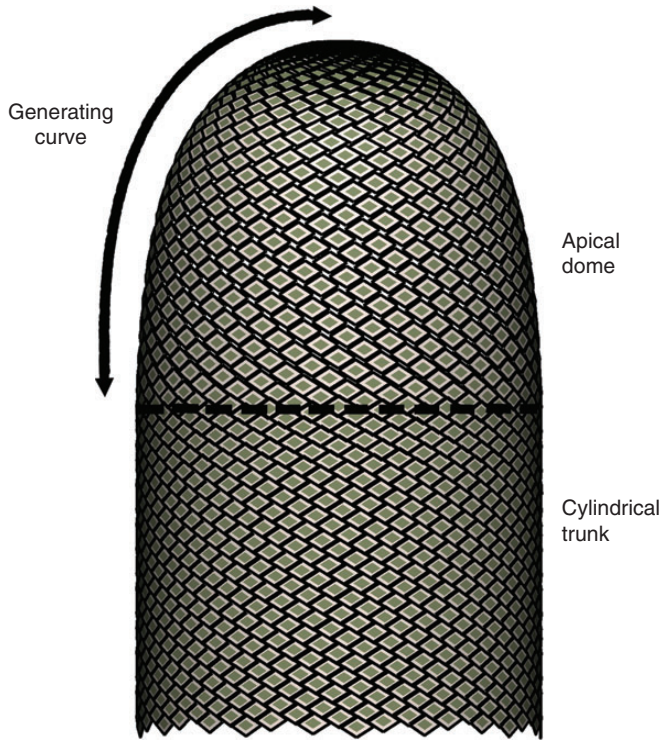


FIG. 3. Geometry of the tree trunk and a sample distribution of leaf bases generated using Ridley's (1986) model. For clarity, leaf bases are larger and less numerous than in the actual grasstree and the full model. The profile of the apical dome is defined by a generating curve. The dome is smoothly connected to the cylindrical trunk. The division between these two regions is marked by the dashed line.

10–20 mm per year (Lamont *et al.*, 2004). In the context of these data, one time unit in our model is equivalent to 88.5 d and one length unit corresponds to 0.3 m. Our virtual tree started at a height of 1.62 m and reached a height of 2.52 m. This corresponds to a 60-year simulation period with the tree starting at the age of 110 years and reaching 170 years.

According to our observations, the divergence angle, φ , in young grasstree seedlings (Fig. 1) is close to 137.5° , the golden angle value found in many plant species, and we assumed this divergence angle in our model. The radius of the tree trunk during the simulation increased from 11 to 29 cm, the latter value approximating that observed in trees. We assumed that leaf bases had an area of $\sim 30 \text{ mm}^2$, which is consistent with the reported size of grasstree leaves (Lamont *et al.*, 2004). We measured the number of leaf bases that a horizontal line drawn across the trunk intersected and found ~ 37 bases (Fig. 4E, F), and the angle between parastichies approximated the measured angle of 57° (Fig. 4A–D).

We simulated irregularities in the trunk form, possibly related to the sites of inflorescences, as a periodic increase in the trunk diameter ('bulging') below the apical dome, yielding different leaf base aspect ratios (Fig. 4G–I). This was done by increasing the radial position of the affected masses according to a piecewise sinusoidal function, taking a single maximum at the site of the bulge and a value of zero away from the bulge. The non-zero portion of the function was a squared sine function with period scaled to match the extent of the bulging region

along the trunk, thus guaranteeing a smooth transition to zero at the edges of the functions support.

Fracture simulation. Secondary growth pushes leaf bases outwards, which was modelled by gradually increasing the distance of the leaf bases from the tree axis. For the purpose of fracture pattern formation, we represented leaf bases as masses and the resin connections as (Hookean) springs, connecting each base to its four nearest neighbours. Figure 5A shows the neighbouring leaf bases represented as green masses connected by springs. In addition, each mass was connected to its original position on the surface of the trunk by an 'anchor' spring, restricting the range of possible displacements of the mass (Fig. 5B). As the tree grew in radius, the springs between leaf bases (and possibly some anchor springs) stretched. Whenever the tension of a spring connecting two leaf bases exceeded a critical value, f_{\max} , the springs would break. Broken springs were removed from the simulation, leading to the formation of cracks, and bark patches were formed by the leaf bases interconnected by the remaining springs.

The force with which a spring attached to a leaf base at a point \mathbf{x}_p acts on a leaf base q positioned at \mathbf{x}_q is given by

$$\mathbf{f}_{q,p} = -\frac{k(l_{q,p} - \|\mathbf{x}_p - \mathbf{x}_q\|)(\mathbf{x}_p - \mathbf{x}_q)}{\|\mathbf{x}_p - \mathbf{x}_q\|} \quad (1)$$

where k is the elasticity constant for neighbouring springs. The rest lengths of the springs, $l_{q,p}$, between the adjacent leaf bases was assumed to be equal to the distances between the bases at the time of their transition from the apical dome to the trunk. This implies that leaf bases initiated later in the simulation, when the radius of the tree trunk was larger, and those occurring in the bulging regions had larger rest lengths. Anchor springs were assumed to have zero rest length, which simplified the above formula to

$$\mathbf{f}_{q,s} = -c(\mathbf{x}_s - \mathbf{x}_q) \quad (2)$$

where c is the elasticity constant for secondary growth springs and \mathbf{x}_s is the original position of the leaf base on the trunk. The damping force is given by the equation

$$\mathbf{f}_{q,d} = -b\mathbf{v}_q \quad (3)$$

where \mathbf{v}_q is the velocity of mass q and b is the damping constant. Due to the physical nature of our system (leaf bases glued by resin), we assumed that the system was over-damped [$b > 2\sqrt{(km_q)}$], where m_q is the mass of element q].

The total force acting on the leaf base q is the sum of the spring and the damping forces:

$$\mathbf{F}_q = \mathbf{f}_{q,s} + \mathbf{f}_{q,1} + \mathbf{f}_{q,2} + \mathbf{f}_{q,3} + \mathbf{f}_{q,4} + \mathbf{f}_{q,d} \quad (4)$$

where $\mathbf{f}_{q,j}$ ($j = 1, 2, 3, 4$) correspond to the springs connecting q to the adjacent bases.

Although grasstree growth is a slow process, numerically we considered it as a dynamic system. The positions of each of the masses in the system were simulated by solving the system of

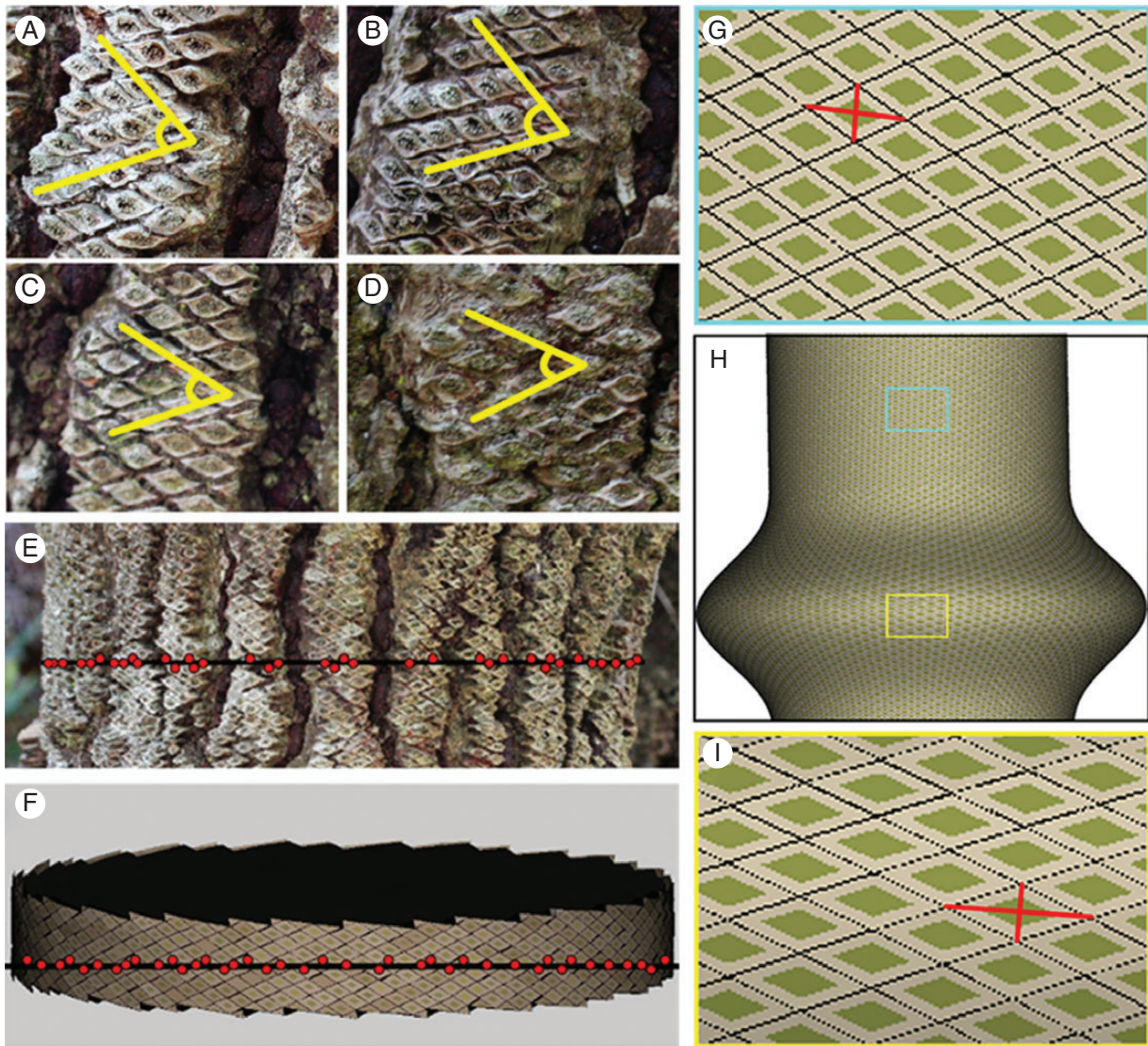


FIG. 4. Estimation of the parameters and geometry of the phyllotactic pattern. (A–D) Measurements of the angle between parastichies ($\sim 57^\circ$) for four different trees/tree sections. (E–F) Comparison of the number of leaf bases intersected by a horizontal line in a grasstree (E) (~ 37) and in the model (F) (~ 40). (H) Calibrated distribution of leaf bases in the regular (blue) and bulged (yellow) segment of the trunk. Leaf bases at the bulge are stretched horizontally (I) compared with regions away from the bulge (G).

differential equations

$$m_q \frac{dv_q}{dt} = F_q \quad (5)$$

$$\frac{dx_q}{dt} = v_q \quad (6)$$

using the Euler–Cromer method (Giordano and Nakanishi, 2005):

$$v_q(t + \Delta t) = \frac{F_q(t)}{m_q} \Delta t + v_q(t) \quad (7)$$

$$x_q(t + \Delta t) = v_q(t + \Delta t) \Delta t + x_q(t) \quad (8)$$

The mass index q runs from $q = 1$ to $n(t)$, where $n(t)$ is the total number of leaf bases present in the trunk at a given time; Δt is a time step used for integration and chosen so that the system is able to reach convergence. Each mass q was constrained to lie on the surface of the trunk. This constraint was enforced by updating $x_q(t)$ according to

$$x_q(t) \rightarrow C + (r_i + G\sqrt{t}) \frac{(x_q(t) - C)}{\|x_q(t) - C\|} \quad (9)$$

where C is the position along the trunk axis at the height of leaf base q , r_i is the initial radius of the trunk and G controls the rate of secondary growth. The anchor points that connect leaf bases to the trunk were constrained to the trunk surface in the same manner. Parameter values used in the model are summarized in Table 1.

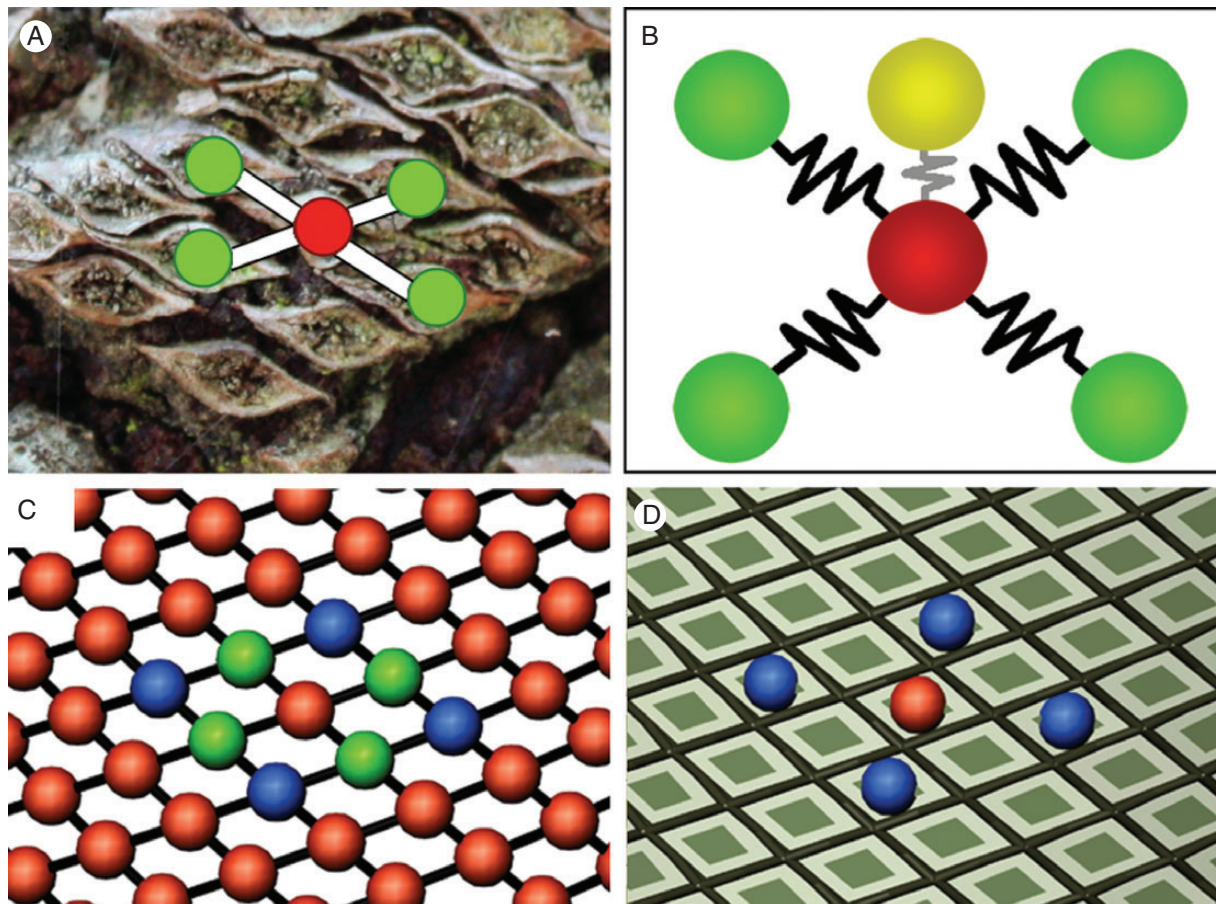


FIG. 5. Mass-spring representation of grasstree bark. (A) Leaf bases are approximated as masses (circles) and the resin connections as springs (white connecting lines). (B) Each mass (red sphere) is connected by springs to four neighbours (green spheres) and to an anchoring point (yellow sphere). (C) Masses and springs are arranged into a lattice. (D) The surface of the trunk is partitioned into individual leaf base elements, and the four vertices of each leaf base are placed half the distance between the red mass and a blue mass.

Visual presentation of the model. For visual completeness, full leaves were incorporated into the model. Leaves were modelled as generalized cylinders with the area of the diamond-shaped cross-section decreasing towards the endpoints. The shape and size of the leaf bases were calculated so that the mesh of masses and springs completely partitioned the surface of the trunk into rhomboids (Fig. 5C, D) at the moment when the leaf bases moved from the apical dome to the trunk. Leaf bending due to gravity was approximated by gradually turning the leaf downwards along its axis (Prusinkiewicz and Lindenmayer, 1990). As the leaves aged, they turned brown and to simulate the role of a forest fire the majority of the older leaves were eventually removed, leaving only the base.

Statistical analysis of observed and simulated patterns

Materials. We analysed 30 photographs of grasstrees (taken on Mount Kiangarow, Queensland, in December 2009) and magnified certain segments of their trunks. The bark patterns were clearly visible in most trees, but the individual patches were often partially weathered or covered by an outgrowth of mosses or lichens, which made the precise identification and the recording of individual leaf bases difficult. Consequently, we have focused on different areas of a single tree, in which all

bases are remarkably visible. We have complemented these results with an analysis of the distribution of bases and fractures.

Data acquisition. The observed patches were digitized manually from the photographs, using custom software devised for this purpose (Fig. 6). Positions of leaf bases were specified by placing a point at the centre of each leaf base using a mouse, and recording the (x, y) coordinates of this point in the plane of the image. In order to minimize the impact of projective distortions, we only considered areas of the trunk approximately facing the camera. This approximation was possible because the horizontal spread of individual patches was much smaller than the diameter of the trunk. The clustering of leaf bases into patches was estimated by visual inspection, with all bases assigned to the same patch indicated by the same point colour (Fig. 6A, D). This assignment was straightforward in the case of patches separated by large gaps. Narrow gaps were more difficult to classify, often raising the question of whether the small patches were connected to other patches or not. In order to avoid a possible impact of ambiguous patches, we ignored them in our analysis.

For simulated data (Fig. 7), patches were extracted computationally, based on the graph of connections (unbroken springs) between leaf bases. Each patch corresponded to a single

TABLE 1. Parameter values used in the grasstree model

Parameter	Symbol	Value
Force threshold for breaking in the straight sections of the trunk	f_{\max} : straight	0.005 force units
Force threshold for breaking in the straight sections of the trunk	f_{\max} : bulge	0.006 force units
Initial radius	r_i	0.35 (10 cm)
Vertical displacement for the initial cylindrical trunk.	h	0.00012 (0.036 mm)
Index offsets to neighbouring masses (green masses in Fig. 3)		$\pm 55, \pm 89$
Index offsets to masses used to partition the surface into leaf bases (blue masses in Fig. 3C, D)		$\pm 34, \pm 144$
Time step	Δt	0.01 (21 h)
Elasticity constant for neighbouring springs	k	1.0 force/distance units (1.3 force m^{-1})
Elasticity constant for secondary growth springs	c	0.03 force/distance units (0.1 force m^{-1})
Damping constant	b	2.0 force/velocity units
Constant for secondary growth on the straight sections	G : straight	$0.04 \text{ distance}/(\text{time unit})^{1/2}$
Constant for secondary growth	G : bulge	$0.04 \text{ (ends)} - 0.02 \text{ (peak of the bulge) in distance}/(\text{time unit})^{1/2}$
Spring mass	m_q	1.0 mass units

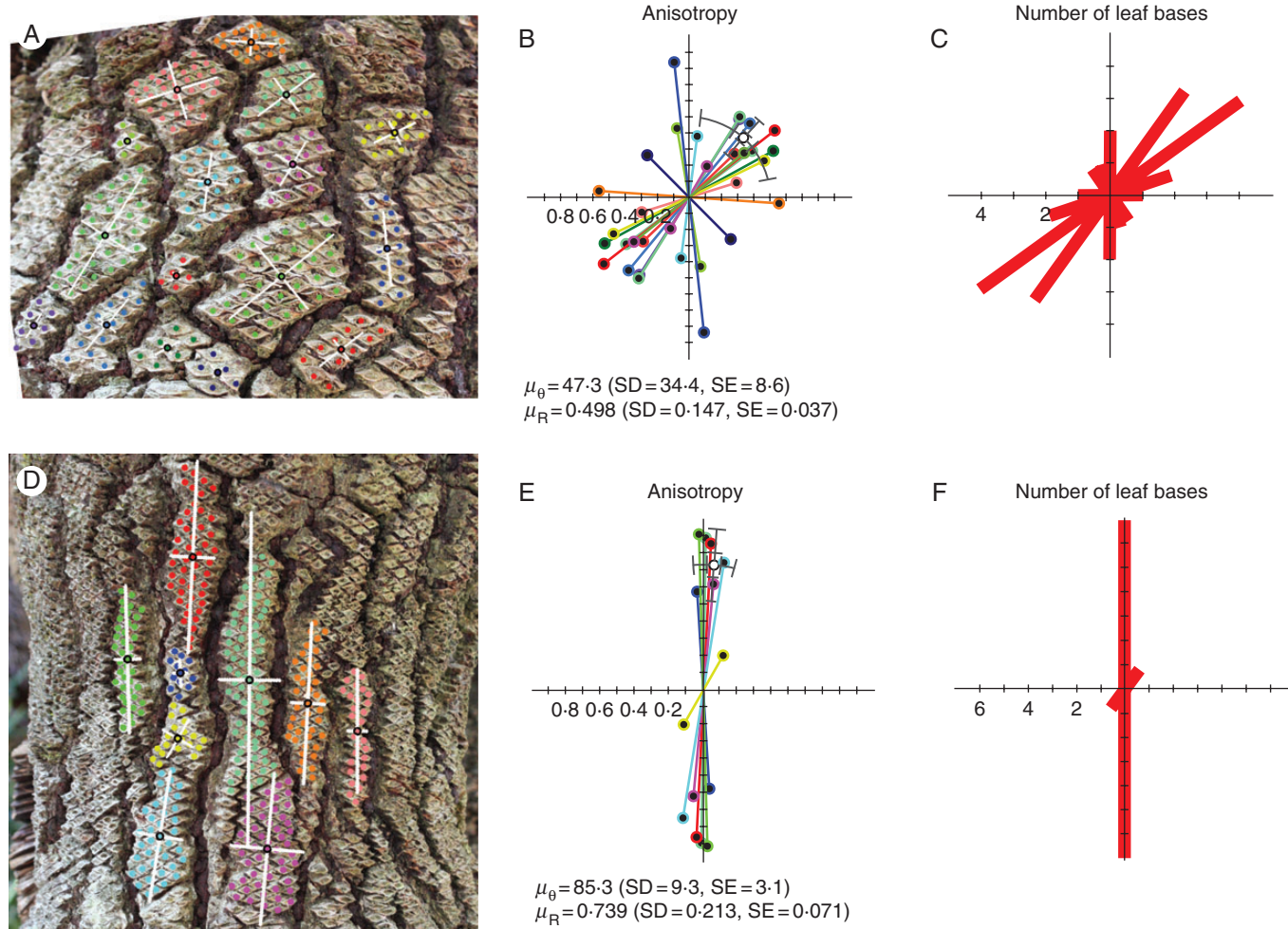


FIG. 6. Digitized bark patches from two photographs of a grasstree trunk (A, D), along with statistics characterizing these patches (B, C, E, F). Image (A) has 16 digitized patches and (B) has nine. Leaf base positions (coloured disks), mean position (coloured disks with black borders) and principal components (white lines) are shown for each patch (A, D). The same colour is used for all leaf bases in a given patch. Radial plots (B, E) show the orientation (angle) and anisotropy (radius) of each patch. Angles are measured with respect to the up-direction of the trunk ($\theta = 90^\circ$). Anisotropy values range from 0 to 1, with the increments of 0.1 marked by ticks. The colour of each data point matches the corresponding patch in (A) or (D). Numerical values for the mean orientation μ_θ [computed using the procedure described by Fisher (1985)] and anisotropy μ_R are provided for each plot along with their standard deviation and error. The histograms in (C, F) show the orientations of individual patches grouped into 10 bins of 18° each. The radius of each bin shows the number of patches within each bin (one-patch increments are marked).

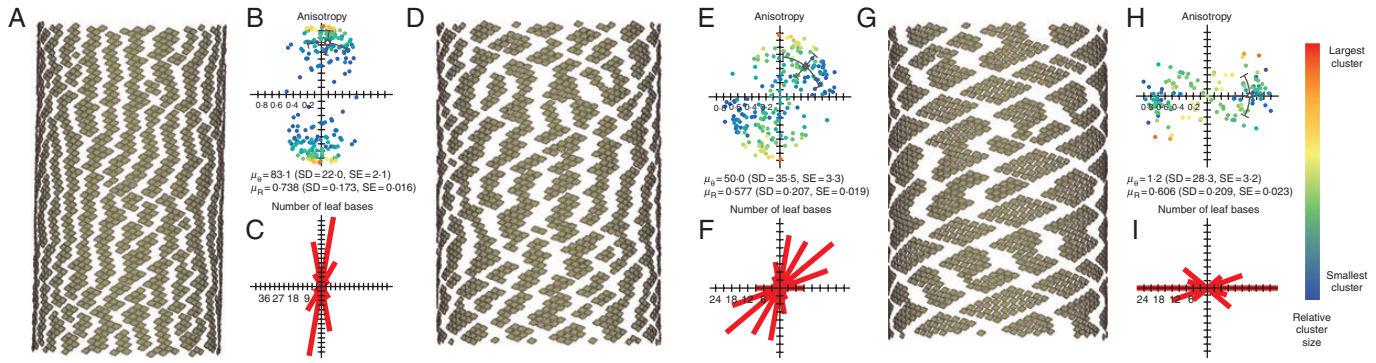


FIG. 7. Simulated patterns produced by the varying parameters between the two regimes of pattern formation described in the text (A, D, G) and statistics computed from these patterns (B, C, E, F, H, I). The radial plots (B, E, H) show orientation and anisotropy as for Fig. 6 with two exceptions. First, corresponding data points in the upper and lower half-planes are no longer connected by a line. Second, the colour of each data point indicates the number of leaf bases in the corresponding patch, according to the colour ramp shown at the right of the figure. The histograms (C, F, I) show the number of patches falling into each angular bin as in Fig. 6 (with three-patch increments marked). (A–C) The patches ($n = 110$) in a simulation of the first regime (A) produce the radial plot in (B) and the histogram in (C). (D–F) The patches ($n = 115$) in a simulation using the parameters between those of the first and second regimes (D) produce the radial plot in (E) and the histogram in (F). (G–H) The patches ($n = 80$) in a simulation of the second regime (G) produce the radial plot in (H) and the histogram in (I).

connected component of the graph. Consistent with the method for acquiring experimental data, we mapped each patch into a tangent plane passing through the centroid of the patch and recorded the coordinates of leaf bases in this plane. We focused our analysis on the models in which the spread of patches in the horizontal direction was limited, although patches with spreads commensurate with the diameter of the cylinder could also be generated for some parameter values. Furthermore, we disregarded patches with fewer than seven leaf bases in order to be consistent with the elimination of ambiguous patches in the analysis of observational data.

Pattern characterization. We recorded the size (in number of leaf bases) of each observed or simulated patch, and computed the orientation and anisotropy of each patch by performing a principal component analysis (Jolliffe, 2012) on the positions $\{(x_o, y_o), (x_I, y_I), \dots, (x_k, y_k)\}$ of leaf bases within this patch. To this end, we computed the pairwise covariances of the spatial components of leaf base positions and arranged them into the covariance matrix

$$\Sigma = \begin{bmatrix} \text{cov}(X, X) & \text{cov}(X, Y) \\ \text{cov}(Y, X) & \text{cov}(Y, Y) \end{bmatrix} \quad (10)$$

From Σ , we extracted the eigenvalues of the covariance matrix, λ_1 and λ_2 , and their corresponding eigenvectors: α_1 and α_2 . The eigenvectors are the principal components (PCs) of the spatial distribution of leaf bases, and the eigenvalues characterize the portion of the total variance of the point set along each PC. In this setting, the first (larger) PC, λ_1 , describes the primary orientation in which the leaf bases within a patch are distributed. We visualize this orientation as a line aligned with the first PC, passing through the mean of the leaf base positions (Fig. 6A, D). The second principal component, λ_2 , characterizes the spread of the leaf bases in the direction orthogonal to the first PC. The ratio

$$A = \frac{\lambda_1}{\lambda_1 + \lambda_2} \quad (11)$$

describes the anisotropy of this patch, ranging from $A = 1/2$ for a perfectly isotropic patch (the same spread in the first and the

second principal direction) to $A = 1$ for a perfectly anisotropic patch (all bases aligned in the principal direction) (Pauly et al., 2002). We map these values to the interval $[0, 1]$ using the reassignment $A \rightarrow 2A - 1$ to make the differences in anisotropy more clearly represented in plots. A similar measure was recently used to quantify anisotropy of patterns (of road networks) by Courtat et al. (2011).

Pattern comparisons. The key objective of this analysis was to objectively verify that our models of elongated and reticulate bark patterns were close to those observed in grasstrees, while being relatively distant from each other. Specifically, we compared four classes of pattern: real elongated patterns, simulated elongated patterns, real reticulate patterns and simulated reticulate patterns. To this end, we employed quartet analysis (Bandelt and Dress, 1986; Schmidt et al., 1996; Strimmer and von Haeseler, 1996), which provides a method for inferring qualitative relations from quantitative measurements (Bandelt and Dress, 1986) and can be used to compare shapes (Huang et al., 2013). To compare distances d between four patterns, P, Q, R and S (Fig. 8A), we formed a graph connecting the three closest pairs of patterns with edges (Fig. 8B, C). If the two closest pairs (coloured green) were disjoint, a reliable proximity of patterns in each pair could be inferred. For instance, in the case shown in Fig. 8B, the quartet analysis indicates that the pairs PQ and RS were relatively close compared with the distance between the pairs. In contrast, a reliable pairing could not be established in the example shown in Fig. 8C, because pairs PQ and PR were not disjoint.

As the distance d required for quartet analysis, we employed the Hellinger distance between two normal distributions (Korostelev and Korosteleva, 2011). Given distribution P with mean μ_P and standard deviation SD_P , and distribution Q with mean μ_Q and standard deviation SD_Q , this distance is defined as

$$d(P, Q) = \sqrt{(1 - \beta e^\gamma)} \quad (12)$$

where

$$\beta = \sqrt{\frac{2(SD_P)(SD_Q)}{SD_P^2 + SD_Q^2}} \quad (13)$$

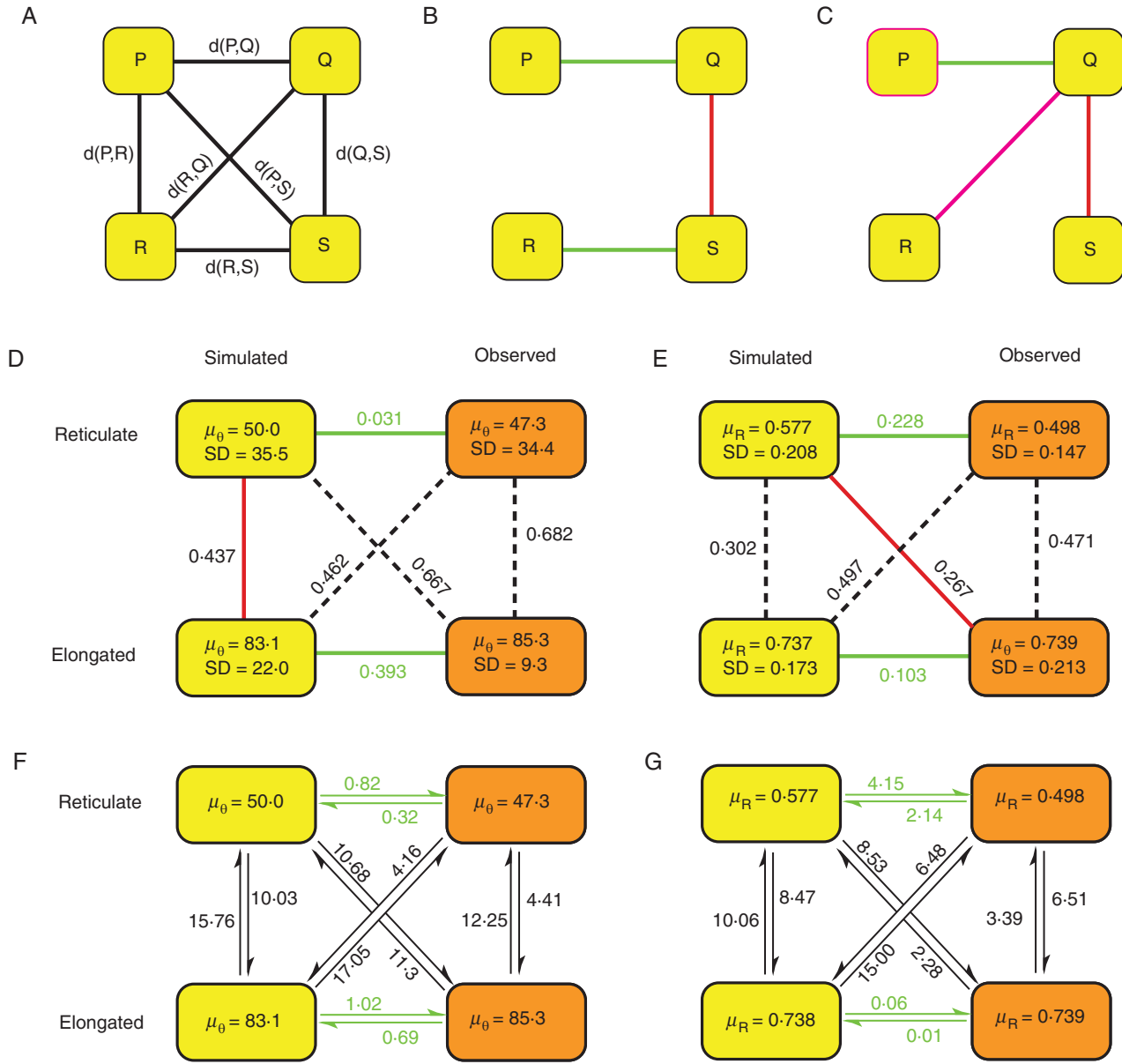


FIG. 8. Inference of qualitative relationships from quantitative data using quartets. (A) Quartet analysis depends on the pairwise distances between P, Q, R and S, as described in the text. (B) Example of a valid quartet. (C) Example of an invalid quartet. In both examples, the three longest edges have been removed. Of the three remaining edges, the two shortest are coloured green and the remaining edge is red. (D, E) Quartet analysis applied to the distribution of orientations (D) and anisotropy values (E). The data in yellow boxes were obtained from the simulations in Fig. 7 (D–F for top left and A–C for bottom left), and the data in orange boxes were obtained from the digitized patches in Fig. 6 (A–C for top right and D–F for bottom right). The pairwise distance between distributions is shown adjacent to each edge. In both columns, the two shortest edges (green) pair the simulated and observed patterns of the same type, while the third shortest edge (red) spans the two pairs. The three longest edges are depicted using dotted lines. (F, G) Differences d_P between the means of the distributions from (D, E), expressed as multiples of the standard errors. The directed edge from P to Q uses the standard error of P (and vice versa). The outgoing edge from each box with the smallest numerical value is coloured green, and induces a pairing between simulated and observed patterns of the same type.

and

$$\gamma = -\frac{1}{4} \frac{(\mu_P - \mu_Q)^2}{SD_P^2 + SD_Q^2} \quad (14)$$

The Hellinger distance increases from 0 to 1 as the differences between distributions increase.

We further analysed the relation between the four distributions by comparing the pairwise distance between means measured in terms of the standard error of each distribution. More precisely,

for each distribution P we computed the difference between its mean μ_P and that of each remaining distribution Q, μ_Q , in terms of the standard error SE_P at P:

$$d_P(P, Q) = \frac{|\mu_Q - \mu_P|}{SE_P} \quad (15)$$

The distance $d_P(P, Q)$ measures the difference between the two means in terms of the standard error of the mean of P, and is

thus inversely related to the probability that the mean μ_Q could be generated by the same probability distribution as P . The advantage of this measure is its intuitive character, stemming from the direct relation between standard error and statistical significance. However, in contrast to the Hellinger distance, this difference d_P is asymmetrical [$d_P(P, Q) \neq d_Q(Q, P)$] and thus does not formally satisfy the definition of distance, which is assumed in the quartet analysis.

RESULTS

Parameter space exploration

The effect of parameters on leaf base patches produced by the model was examined in a simplified setting, with a trunk segment consisting of 3000 leaf bases growing radially as described by eqn (9). An exploration of the model parameters in this setting revealed a range of patterns spanning two extreme regimes (parameters are given in Table 2).

The first regime was characterized by a pattern of patches that were predominantly vertical (perpendicular to the main direction of trunk growth) (Fig. 7A–C, Supplementary Data Video S1). Pattern formation began with a large number of small, mostly vertical cracks, which subsequently connected. As a result, the bark layer was partitioned into predominantly vertical patches. The patches that departed from a strictly vertical orientation split into smaller sub-patches that were more vertical. The overall orientation of patches thus became increasingly vertical, the larger patches being more vertical than the smaller ones (Fig. 7B, C).

The second regime resulted from an increase in the threshold for springs to break (parameter f_{\max}), combined with a decrease in the growth rate (parameter G). These changes imply that leaf bases are more likely to be significantly displaced before being divided by cracks into separate patches. A pattern of approximately diamond-shaped patches resulted (Fig. 7G, H, Supplementary Data Video S2). This pattern was initiated by a small number of long diagonal cracks that wound around the trunk in the direction of the steeper parastichy (fractures

between bases connected by the shallow parastichy) and divided the leaf bases into oblique strips. The strips subsequently split along the shallow parastichy, forming numerous diamond-shaped patches. The average orientation of the first principal component, α_1 (i.e. the axis along which the patch was most elongated), was 1.2° , which is approximately horizontal. Almost all of the individual orientations fell within 45° of the average. As the trunk grew further, this initial pattern was hierarchically elaborated by the alternate splitting of patches along the parastichies. This hierarchy preserved the approximately horizontal orientation of the first PC (Fig. 7H, I), the longest patches aligning with the direction of the shallow parastichy.

We also observed that independently varying each of the two parameters responsible for the change between the two regimes had distinct, and continuous, effects on the characteristics of the final pattern (Fig. 9). Decreasing the growth rate, G , transforms predominately vertical fractures into fractures that tend to run diagonally, along the parastichies. Increasing the force threshold for breaking, f_{\max} , increases the size of patches. Particular choices of these parameters suffice to reproduce the class of patterns exhibited by grasstrees in nature.

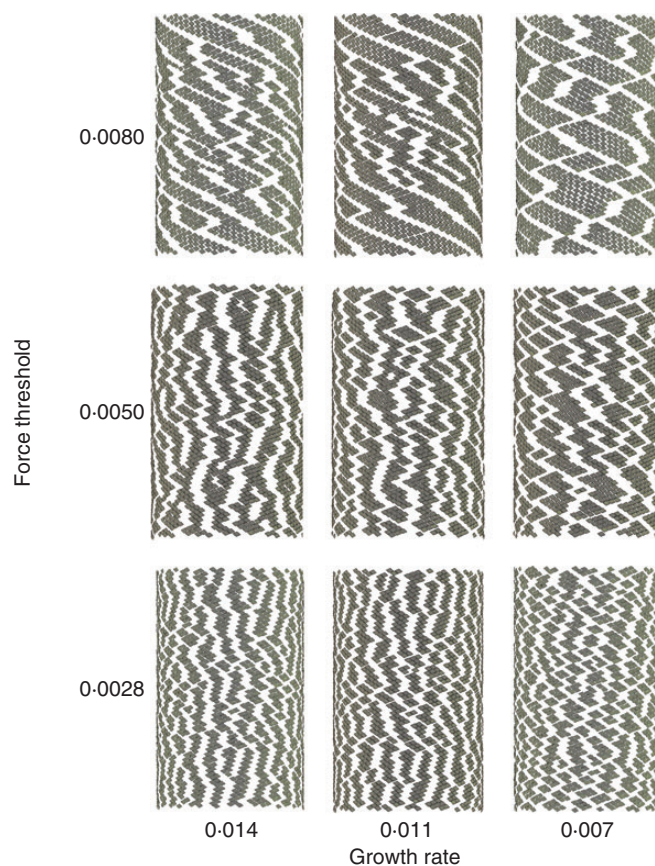


FIG. 9. A 2-D parameter space exploration of the simplified model. The growth rate G is increased for each column from left to right, but is constant for each column. The force threshold f_{\max} is increased for each row from bottom to top, but is constant for each row. The bottom left image uses the same parameters as Fig. 7A, the middle image (second column, second row) uses the same parameters as Fig. 7D and the top right image uses the same parameters as Fig. 7G–I. These parameter values are provided in Table 2.

TABLE 2. Parameter values used in test simulations

Parameter	Symbol	Value
Force threshold for breaking	f_{\max}	0.0028: vertical (Fig. 7A–C) 0.005: reticulate (Fig. 7D–F) 0.008: diamond (Fig. 7G–I) in force units
Initial radius	r_i	0.2 (6 cm)
Vertical displacement	H	0.0005
Index offsets to neighbouring masses		$\pm 21, \pm 34$
Time step	Δt	0.01 (21 h)
Elasticity constant for neighbouring springs	k	0.4 force/distance units (0.12 force m^{-1})
Elasticity constant for secondary growth springs	c	0.1 force/distance units (0.03 force m^{-1})
Damping constant	b	5.0 force/velocity units
Constant for secondary growth	G	0.014: vertical (Fig. 7A–C) 0.011: reticulate (Fig. 7D–F) 0.007: diamond (Fig. 7G–I) in distance/(time unit) ^{1/2}
Spring mass	m_q	1.0: mass units



FIG. 10. Selected images from the grasstree simulation showing various stages of development. The left image starts with 45 000 leaf base elements and corresponds to an age of 110 years, and the final image contains 70 000 leaf base elements and corresponds to an age of 170 years. Parameter values are summarized in Table 1.

Comparison of real and simulated patterns

Visual comparisons and statistical analysis showed that patches emerging in the first regime were similar to the elongated forms observed in the grasstrees in our study (compare Fig. 6D–F with Fig. 7A–C). In particular, both the observed and the simulated patches were highly elongated and almost vertical. In contrast, the pattern generated in the second regime (Fig. 7G–H) was visually similar to the reticulate patterns observed in grasstrees. This visual similarity occurred in spite of a difference in the statistical properties of the two patterns: the average orientation of patches in the model was nearly horizontal, while in the tree it was approximately 47° with respect to a horizontal reference axis. We observed, however, that linearly varying parameters between those defining the first and the second regime resulted in continuous variation in the produced patterns (Fig. 9). A pattern of patches with parameters set intermediately between those for the first and second regime, at 43% of the difference, represents a good fit to the data obtained for the reticulate patterns (Fig. 7D–F, Supplementary Data Video S3).

To further understand the relations between the patterns and their models, we performed separate quartet analyses of the distributions of orientations (Fig. 8D) and anisotropy values (Fig. 8E) of the patterns observed in grasstrees (elongated in Fig. 6D–F and reticulate in Fig. 6A–C) and their models (elongated in Fig. 7A–C and reticulate in Fig. D–F). Furthermore, we performed the corresponding quartet-like analyses using the asymmetrical differences d_p (Fig. 8F, G), comparing the outgoing edges for each box. The four analyses yielded the same qualitative results, indicating that the models of elongated and reticulate patterns were close to the corresponding observed patterns, while the distances between elongated and reticulate patterns were comparatively larger.

Integrative model

Based on the preceding parameter exploration, we implemented a model of the entire above-ground part of the grasstree

(Fig. 10). The model accounts for primary growth, which includes the arrangement of leaves in a spiral phyllotactic pattern, phyllotactic and secondary growth, which leads to the fractured pattern of the bark-like layer of leaf bases. Bulges were introduced to represent irregularities in the trunk. This had a secondary effect of producing stretched leaf bases and a change in leaf base shape similar to that observed in our data from actual grasstrees (Fig. 2B, C). This change in geometry, however, was insufficient to reliably reproduce the different fracture patterns we had observed. Incorporating the results of the parameter space exploration made it possible to reproduce both elongated and reticulate patterns in the same tree. This was achieved by increasing the force threshold for breaking and decreasing the growth rate in the bulging regions (making the magnitude of the bulge decrease with time). Figure 11 shows a comparison of the bark fracture patterns obtained in the model compared with images of the real tree (same images as Fig. 2) showing the two different fracture regimes.

DISCUSSION

We have analysed the patterns of leaf bases forming the bark-like outside layer of the trunks of old grasstrees. These patterns result from a partitioning of leaf bases, initially arranged into a spiral phyllotactic pattern, into patches. Within each patch, the bases are interconnected by resin. Across the crevices these connections are missing.

We observed two variants of these patterns. The first variant is characterized by vertically elongated bark patches and crevices. The second variant is a reticulate pattern of patches and crevices. We used a principal component analysis to characterize both variants quantitatively in terms of the orientation and degree of anisotropy of their constituent patches. Our analysis confirmed the visual observation that patches in the first variant of the pattern are highly anisotropic and have a mean orientation close to vertical, and that the orientation of individual patches is close

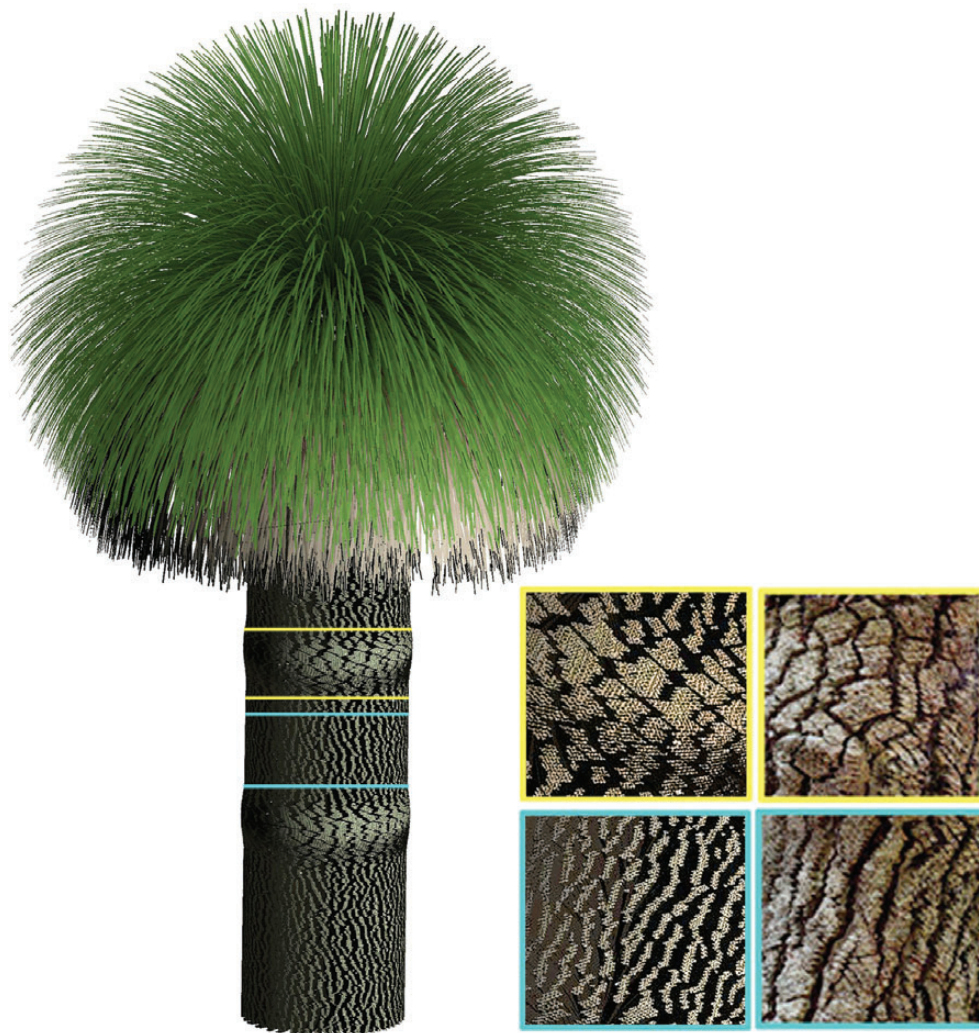


FIG. 11. Bark patterns in the simulation compared with those observed in a real grasstree (the same images as in Fig. 2B, C). Regions near bulges or kinks in the trunk (yellow boxes) have horizontally stretched bases and more diagonal fractures compared with the regions away from the kinks (blue boxes), which have primarily vertical fractures. The inset images of the simulated bark patterns shown on the left are segments of the regions outlined on the tree model and have been rotated and colour-adjusted to better match the real images on the right.

to the mean. In contrast, patches in the second variant of the pattern are more isotropic, have a mean orientation of $\sim 47^\circ$ with respect to a horizontal reference axis, and the orientations of individual patches have greater variance ($SD = 34.4^\circ$, compared with 9.3° for the first variant).

Addressing the question of the developmental origin of the observed patterns, we hypothesized that they may result from the mechanical fracturing of the resin between some leaf bases, while the stresses acting on the resin are induced by the expansion of the bark-like layer due to the secondary growth of the trunk. To explore the plausibility of this hypothesis, we constructed a simple biomechanical simulation model. We have shown that, for different model parameters, this model produces patterns that are visually and statistically similar to both the elongated and the reticulate patterns observed in real trees.

In particular, decreasing the growth rate and increasing the force threshold for the springs to break results in a transition from elongated fractures to a more reticulate pattern. An initial physical analysis of the modelled equations elucidates the

impact of these parameters (see Supplementary Data Extended Results) and indicates that the rate of energy dissipation plays a significant role in patterning. This analysis shows that the damping constant has a significant effect on the number of initial fractures occurring on the surface of the trunk and, together with the growth rate, determines the energy dissipation rate. The number of initial fractures is indicative of the system preferring straight fractures (with a large number of initial fractures) or diagonal fractures (with a smaller number of initial fractures). Interestingly, the number of fractures appears to obey a power law relationship with the energy loss rate (see Supplementary Fig. S1), indicating that the model of grasstree leaf bases behaves like a brittle material. This initial work is promising, but further work is required to fully characterize the relation between the patterns and the physical parameters.

Due to the simplicity of the model, it is difficult to attribute a specific meaning to these parameter changes, but they nevertheless point to physical differences in the two regions as the cause of the different patterns. For example, protrusions on the tree

arising from sympodial growth may experience different rates of secondary growth. Furthermore, regions with larger leaf bases may exhibit different fracturing patterns due a larger area of contact between neighbouring bases, leading to a higher force threshold for breaking.

Our model was devised under strong simplifying assumptions. For example, the one-dimensional springs used in our model cannot capture shear stresses that may occur in the resin between leaf bases. Furthermore, all springs in our model are linear (they obey Hooke's law up to the point of breaking), although grasstree resin may exhibit a more complicated non-linear, plastic and/or viscoelastic (Gross and Seelig, 2011) behaviour. Also, the resin can behave differently at different locations on the tree (Bray, 1905) and vary among species (Birch and Dahl, 1974). Constructing a model of the bark-like patterning in grasstrees based on measured mechanical properties of resin and accounting for the geometry of leaf bases is an open problem, interesting at least from the methodological point of view.

The appeal of using the grasstree as a model for bark-like pattern formation lies in the discrete structure of its layer of leaf bases, which we have abstracted as a simple mass-spring model. This model was adequate to support our general hypothesis that the patterns observed in the grasstree bark-like layer – and, perhaps, in the bark of other trees – may be explained in terms of mechanical fractures driven by secondary growth. Although the generality of our result is limited by the unusual structure of grasstree bark, it supports the hypothesis that bark pattern formation is primarily a biomechanical phenomenon. From a broader perspective, our results increase the spectrum of morphogenetic phenomena in which biomechanics and properties of space, rather than detailed genetic patterning, play a key role (Prusinkiewicz and de Reuille, 2010).

SUPPLEMENTARY DATA

Supplementary data are available online at www.aob.oxfordjournals.org and consist of the following. Video S1: development of a pattern with vertically elongated patches and fractures (Fig. 7A–C). Video S2: development of a pattern with diamond-shaped patches and fractures (Fig. 7G–I). Video S3: development of a reticulate pattern (Fig. 7D–F). Extended Results: a discussion presenting further physical analysis of the parameter space, representing an extension of the section ‘Parameter space exploration’ in the Results.

ACKNOWLEDGEMENTS

Thanks to Jim Hanan, Peter Room and Birgit Loch for introducing P.P. to the beauty of grasstrees and for help in acquiring grasstree data. This work was supported by an Undergraduate Student Research Award (H.D.) and a Discovery Grant (P.P.) from the National Sciences and Engineering Research Council of Canada.

LITERATURE CITED

- Bandelt HJ, Dress A. 1986.** Reconstructing the shape of a tree from observed dissimilarity data. *Advances in Applied Mathematics* **3**: 309–343.
- Birch AJ, Dahl CJ. 1974.** Some constituents of the resin of *Xanthorrhoea preissii*, *australis* and *hastile*. *Australian Journal of Chemistry* **27**: 331–344.
- Bohn S, Platkiewicz J, Andreotti B, Adda-Bedia M, Couder Y. 2005.** Hierarchical crack pattern as formed by successive domain divisions. II. From disordered to deterministic behavior. *Physical Review E* **71**: 046215.

- Bray J. 1905.** *Grasstree resin*. Sydney Morning Herald, 15 December, p. 15.
- Bülow-Olsen A, Just J, Liddle MJ. 1982.** Growth and flowering history of *Xanthorrhoea johnsonii* Lee (Liliaceae) in Toohey Forest Queensland. *Botanical Journal of the Linnean Society* **84**: 195–207.
- Colangelo W, Lamont B, Jones A, Ward D, Bombardieri S. 2002.** The anatomy and chemistry of the colour bands of grasstree stems (*Xanthorrhoea preissii*) used for plant age and fire history determination. *Annals of Botany* **89**: 605–612.
- Courtat T, Gloaguen C, Douady S. 2011.** Mathematics and morphogenesis of the city: a geometric approach. *Physical Review E* **83**: 036106.
- Erickson RO. 1983.** The geometry of phyllotaxis. In: Dale JE, Milthroe FL, eds. *The growth and functioning of leaves*. Cambridge: Cambridge University Press, 53–88.
- Federl P, Prusinkiewicz P. 1996.** A texture model for cracked surfaces. In: *Proceedings of the Seventh Western Computer Graphics Symposium, 4–6 March 1996*. Panorama, British Columbia, 23–29.
- Federl P, Prusinkiewicz P. 2004.** Finite element model of fracture formation on growing surfaces. In: *Proceedings of Computational Science – ICCS 2004, Part II*. Lecture Notes in Computer Science 3037. Berlin: Springer, 138–145.
- Fisher IN. 1995.** *Statistical analysis of circular data*. Cambridge: Cambridge University Press.
- Gill AM, Ingwersen F. 1976.** Growth of *Xanthorrhoea australis* R. Br. in relation to fire. *Journal of Applied Ecology* **13**: 195–203.
- Giordano NJ, Nakanishi H. 2005.** *Computational physics*, 2nd edn. West Lafayette: Benjamin Cummings.
- Gross D, Seelig T. 2011.** *Fracture mechanics with an introduction to micromechanics*, 2nd edn. Heidelberg: Springer.
- Huang S-S, Shamir A, Shen C-H, Zhang H, Sheffer A, Hu S-M, Cohen-Or D. 2013.** Qualitative organization of collections of shapes via quartet analysis. *ACM Transactions on Graphics* **32**: Article 71.
- Van Iterson G. 1907.** *Mathematische und mikroskopisch-anatomische Studien über Blattstellungen*. Jena: Gustav Fischer.
- Jolliffe I. 2012.** *Principal component analysis*, 2nd edn. Providence, RI: Springer.
- Korostelev A, Korostevea O. 2011.** *Mathematical statistics: asymptotic Minimax theory*. Graduate studies in mathematics, Vol. 119. New York, NY: American Mathematical Society.
- Lamont BB, Wittkuhn R, Korczynskij D. 2004.** Ecology and ecophysiology of grasstrees. *Australian Journal of Botany* **52**: 561–582.
- Morgenstern O, Sokolov IM, Blumen A. 1993.** Analysis of a one-dimensional fracture model. *Journal of Physics A* **26**: 4521–4537.
- Pauly M, Gross M, Kobbelt LP. 2002.** Efficient simplification of point-sampled surfaces. *Proceedings of the Conference on Visualization '02*. Washington, DC: IEEE Computer Society, 163–170.
- Prusinkiewicz P, Barbier de Reuille P. 2010.** Constraints of space in plant development. *Journal of Experimental Botany* **61**: 2117–2129.
- Prusinkiewicz P, Lindenmayer A. 1990.** *The algorithmic beauty of plants*. New York: Springer.
- Prusinkiewicz P, Mündermann L, Karwowski R, Lane B. 2001.** The use of positional information in the modeling of plants. *Proceedings of SIGGRAPH 2001*. New York: ACM SIGGRAPH, 289–300.
- Ridley JN. 1986.** Ideal phyllotaxis on general surfaces of revolution. *Mathematical Biosciences* **79**: 1–24.
- Rudall P. 1991.** Lateral meristems and trunk thickening growth in monocotyledons. *Botanical Review* **57**: 150–163.
- Schmidt HA, Strimmer K, Vingron M, von Haeseler A. 1996.** Tree-Puzzle: maximum likelihood phylogenetic analysis using quartets and parallel computing. *Bioinformatics* **3**: 502–504.
- Shinozaki K, Yoda K, Hozumi K, Kira T. 1964a.** A quantitative analysis of plant form – the pipe model theory. Basic analysis and further evidence of the theory and its application in forest ecology. *Japanese Journal of Ecology* **14**: 97–105.
- Shinozaki K, Yoda K, Hozumi K, Kira T. 1964b.** A quantitative analysis of plant form – the pipe model theory. Further evidence of the theory and its application in forest ecology. *Japanese Journal of Ecology* **14**: 133–139.
- Skjeltorp AT, Meakin P. 1988.** Fracture in microsphere monolayers studied by experiment and computer simulation. *Nature* **335**: 424–426.
- Staff IA. 1968.** A study of the apex and growth patterns in the shoot of *Xanthorrhoea media* R. Br. *Phytomorphology* **18**: 153–165.
- Strimmer K, von Haeseler A. 1996.** Quartet puzzling: a quartet maximum-likelihood method for reconstructing tree topologies. *Molecular Biology and Evolution* **7**: 964–969.